Impact on Sea-Surface Electromagnetic Scattering and Emission Modeling of Recent Progress on the Parameterization of Ocean Surface Roughness, Drag Coefficient, and Whitecap Coverage in High Wind Conditions

Paul A. Hwang

***Abstract*—Ocean surface wind stress is the force generating ocean surface roughness and whitecaps. The surface wind stress is related to the surface wind speed by the drag coefficient. Consequently, the magnitude of roughness and whitecaps calculated from wind speed input depends on the applied drag coefficient formula, which remains uncertain especially for high wind conditions. Because roughness and whitecaps are two major components of the ocean surface response in microwave remote sensing, a clear understanding of the drag coefficient, ocean surface roughness, and whitecap coverage is critical to interpreting the microwave signals emitted or scattered from the ocean surface. In reverse, the microwave signals represent precious data sources of these ocean surface properties [surface wind stress (or equivalently the drag coefficient), surface roughness, and whitecaps] that are difficult to measure with traditional oceanographic instruments, especially in severe weather conditions. This article describes the improvement of ocean surface properties achieved by incorporating microwave remote sensing measurements. In essence, the global data of microwave monostatic and bistatic radar cross sections contribute to the revision of ocean surface roughness spectrum model, and microwave radiometer measurements in tropical cyclones provide clarification regarding the dependence on wind speed of the drag coefficient and whitecap coverage. In return, the calculated excess emissivities and scattering radar cross sections are improved from implementing the updated results of drag coefficient, whitecap coverage, and surface roughness in microwave emission and scattering models.**

***Index Terms*—Brightness temperature (BT), drag coefficient, microwave remote sensing, ocean surface roughness, whitecaps, radar cross section.**

I. Introduction

MICROWAVE remote sensing plays an important role in ocean research and environmental monitoring. The received microwave signals from the ocean surface contain signatures of various oceanographic processes that modify the electromagnetic (EM) emission and scattering at the ocean surface. In particular, ocean surface roughness and whitecap coverage are two main contributors to the received signals in microwave wind sensing. Since surface wind stress drives both surface roughness and whitecaps, microwave signals from the ocean surface are good data sources for investigating the properties of surface roughness, whitecap coverage, and surface wind stress (or equivalently, the drag coefficient).

This article describes some recent progress of modeling the surface roughness, whitecap coverage, and surface wind stress aided by analyzing microwave measurements. Analytical calculations of the expected microwave responses in ocean emission and scattering are then carried out with the updated results of drag coefficient, surface roughness, and whitecap coverage implemented in the ocean emission and scattering models. The upgraded formulations of the ocean surface processes clearly improve the microwave scattering and emission computation results.

Section II describes the treatment of ocean surface roughness. The contributing microwave data sources include scatterometer backscattering normalized radar cross sections (NRCSs) represented by the *Ku*-, *C*-, and *L*-band geophysical model functions (GMFs) and lowpass-filtered mean square slopes (LPMSSs) derived from Global Navigation Satellite System reflectometry (GNSSR) bistatic radar cross sections. The section also describes the treatment of whitecap coverage and surface wind stress, the contributing data sources are microwave radiometer brightness temperature (BT) measurements covering a wide range of microwave frequency, incidence angle, wind speed, and both vertical and horizontal polarizations. Section III discusses the improvements on computing the co- and cross-polarization NRCS and surface emission from the ocean surface through implementing the revised drag coefficient, surface roughness, and whitecap coverage in the scattering and emission models. Section IV summarizes this article.

Manuscript received September 3, 2019; revised February 3, 2020, February 21, 2020, and February 26, 2020; accepted February 26, 2020. Date of publication April 8, 2020; date of current version May 19, 2020. This work was supported by the Office of Naval Research under Grant N0001416WX00044.

The author is with the U.S. Naval Research Laboratory, Washington, DC 20375 USA (e-mail: paul.hwang@nrl.navy.mil).

Digital Object Identifier 10.1109/JSTARS.2020.2977420

II. Surface Roughness and Microwave Scattering

A. Similarity Relationship of Centimeter to Decameter (cmDm) Waves

The wave spectral properties in the cmDm wavelength range are of great importance to microwave remote sensing of the ocean environment. Early attempts to describe the spectral properties of cmDm waves generally rely on extrapolating the ocean surface wind wave spectral models, and appending a relatively simple model for the high-frequency components, e.g., [1]–[8]. The wind wave spectral models address the energetic components near the wave energy spectral peak region, which are typically in the range of deca- to hecto-meter wavelengths. Because the spectral energy decays sharply from the peak region toward the short wavelength components, the spectral peak region is not sensitive to the variation in the cmDm portion of the spectrum. Consequently, the information in the spectral peak region provides little guidance on how to extrapolate toward the cmDm region. There are large differences in the resulting cmDm wave components among different wave spectral models. The discrepancies cannot be resolved easily because of the lack of clear and quantitative understanding of the complicated physical mechanisms governing the dynamics of cmDm waves.

In a major departure from the extrapolation approach, an ocean surface roughness spectrum model [9] is anchored on the similarity function of cmDm waves reported in [10]. The similarity function prescribes the dimensionless spectrum $B(k)$ as a power function of dimensionless surface wind forcing

$$B\left(\frac{u_*}{c};k\right) = A(k)\left(\frac{u_*}{c}\right)^{a(k)} \tag{1}$$

where c is the phase speed of the wave component with wavenumber k, and u_* is the wind friction velocity, which is proportional to the square root of surface wind stress. The wind friction velocity is related to the surface wind speed U_{10} by a drag coefficient C_{10}: $u_* = C_{10}^{0.5}U_{10}$, more discussion on the drag coefficient is given in Section II-C. The properties of a wave spectral component are, therefore, characterized by two factors: the proportionality coefficient $A(k)$ and the exponent $a(k)$.

[The 1-D dimensionless spectrum $B(k)$ is related to the 1-D wave elevation spectrum $F(k)$ by $B(k) = k^3F(k)$, where $F(k) = \int_{-\pi}^{\pi} S(k,\phi)kd\phi$; $S(k,\phi)$ is the 2-D elevation spectrum, that is, $\int_0^\infty F(k)dk$ and $\int_0^\infty \int_{-\pi}^{\pi} S(k,\phi)kdkd\phi$ yield the variance of the surface elevation $\langle\eta^2\rangle$, and ϕ is the wave propagation angle with respect to the wind direction.]

The initial results of $A(k)$ and $a(k)$ are derived from a database of short wind wave spectra measured by fast response wave gauges mounted on a wave-following and free-drifting buoy to alleviate the problem of Doppler frequency shift of short waves caused by surface currents and orbital velocities of long waves [9]–[11]. The field data were collected over about three years in northern Gulf of Mexico, the wind speed range is between 2 and 14 m/s. The k range is between about 0.5 and 320 rad/m for the $A(k)$ and $a(k)$ functions derived from the field data.

Because c and k are related by the surface wave dispersion relationship: $c^2 = g/k + \tau k$, where g is the gravitational acceleration and τ is the surface tension divided by the water density, $B(u_*/c; k)$ is an equivalent representation of the ocean surface roughness spectrum. In practice, a matrix of $B(u_*/c; k)$ is computed for a range of u_* and k with (1). Expressed as $B(u_*, k)$, the result describes the wind response $B(u_*)$ for a given k, or the spectrum $B(k)$ at a given u_*. A unique feature of this spectral design is its accommodation to revision and flexibility to adapt new data sources. Revisions of the roughness spectrum over the years take into account the additional information of ocean surface roughness from remote sensing sources that roughly divide into Bragg resonance and tilting categories, as described in the following.

B. Microwave Radar and Radiometer Data Sources

The similarity relation (1) serves as a vehicle for incorporating microwave radar backscattering measurements into the cmDm wave database. The Bragg resonance scattering mechanism dominates the vertical transmit vertical receive (VV) radar backscattering. Computations show that the Bragg and tilted-Bragg solutions are almost identical for incidence angles in the neighborhood of about 55°±10°, and the NRCS $\sigma_{0\mathrm{VV}}$ can be written as

$$\sigma_{0\mathrm{VV}}(\theta) = 16\pi k_r^4 \cos^4\theta |g_{\mathrm{VV}}(\theta)|^2 S(k_B, 0) \tag{2}$$

where k_r is the radar wavenumber, θ is the incidence angle, $k_B = 2k_r \sin\theta$ is the wavenumber of the Bragg resonance surface wave component, and g_{VV} is the scattering coefficient.

Examples of the $A(k)$ and $a(k)$ retrieved from *Ku*-, *C*-, and *L*-band GMFs are shown in [16, Fig. 4] and [17, Fig. 7]. For *Ku*- and *C*-band, the maximum wind speed is 60 m/s, and for the *L*-band, it is 28 m/s [12]–[15]. In low to moderately high winds ($U_{10} < \sim$15 m/s), the GMF-derived $A(k)$ and $a(k)$ are in good agreement with those obtained from *in situ* wave spectra measured by free-drifting wave gauges. Incorporating the scatterometer NRCS data expands the wind speed coverage to tropical cyclone (TC) conditions. In high winds ($u_*/c > \sim$2.5), the similarity function converges to $B(u_*/c; k) \sim (u_*/c)^{0.75}$; more detail is given in [16] and [17]. In addition to extending the wind speed coverage to TC conditions, the NRCS analysis also increases the wave number coverage from about 320 to 510 rad/m. Furthermore, the environmental condition expands from regional (northern Gulf of Mexico) to global.

The parameter $a(k)$ represents the wind speed sensitivity of a given wave spectral component. There are many papers reporting the wind sensitivity of NRCS or BT as represented by the wind speed exponent; the works in [18] and [19] summarize the results published in 19 papers. These NRCS and BT data extend the wavenumber coverage further to ∼1100 rad/m in the $a(k)$ database. Analytical asymptotic functions are developed to extend the wavenumber coverage of $A(k)$ and $a(k)$ to both lower and higher wavenumbers (from 0 to ∞ rad/m), and the inverse wave age $\omega_\# = U_{10}\omega_p/g = U_{10}/c_p$ is introduced to limit the lower end of the wave number range of the computed wave spectrum [16]. In the abovementioned expression, c and ω are, respectively, wave phase speed and angular frequency, and subscript p represents the wave component at the energy spectral peak. The analysis results of cmDm waves using microwave

NRCSs are in good agreement with those derived from *in situ* wave spectra data, and microwave measurements become part of the surface roughness database.

The resulting surface roughness spectrum function established with $A(k)$ and $a(k)$ results combining *in situ* and microwave analyses is referred to as the H2015 spectrum model [17] in this article. The computed σ_{0VV} for *Ku*-, *C*-, and *L*-band using the H2015 surface roughness model are in good agreement with the *Ku*-, *C*-, and *L*-band GMFs. The NRCS differences (GMFs − EM solutions) for the three frequencies are presented in [17, Fig. 18]. In most cases, the difference is within 2 dB. The *L*-band data employed in [17] covers wind speed up to about 28 m/s for one incidence angle (45°). The more recent report of Aquarius *L*-band GMF [20] has a higher maximum wind speed, to about 32 m/s, and three incidence angles (29°, 38°, and 46°). The computed NRCS using the H2015 spectrum and the new *L*-band GMF are in similarly good agreement. It is clarified that throughout this article, the NRCS solutions of VV and cross-polarization VH (to be discussed in Section III) are based on the second-order small slope approximation (SSA2) discussed in [17].

Recently, several large datasets of LPMSS have been published [21]–[24] in support of the GNSSR TC wind sensing effort. The *L*-band LPMSS is the integrated contribution of waves longer than about 0.6 m. These long-scale (compared to the EM wavelength) surface waves are the tilting facets that cause changes of the local incidence angle to be different from the nominal incidence angle. The LPMSS is especially useful for examining the longer portion of the cmDm waves when combined with a wind wave spectral model accommodating a variable spectral slope [25], [26]. The spectrum model incorporating the modification in the longer portion of the cmDm waves are denoted H2018 here. Another major modification of H2018 is the revised drag coefficient formula that takes into account the recent analyses of microwave radiometer data, as discussed in the following.

C. Drag Coefficient, Whitecap Coverage, and Microwave Radiometer Measurements

Because of the large scatter in the field data of drag coefficient C_{10} and whitecap coverage W_c, there have been many different formulas proposed in the literature [27]–[43]. The friction velocity u_* is used in the parametric model of surface roughness spectrum and in many models of whitecap coverage W_c. As discussed earlier, the friction velocity, which is proportional to the square root of the surface wind stress, relates to wind speed by the drag coefficient; thus, $C_{10}(U_{10})$ and $u_*(U_{10})$ are equivalent representations. Obviously, for a given wind speed different C_{10} formulas produce different surface wind stresses that quantify the ocean surface roughness and whitecap coverage in scattering or emission computation. Open-ocean datasets of drag coefficient and whitecap coverage from different sources are used to study C_{10}, u_*, and W_c [27]–[40], many of the drag coefficient measurements are obtained inside hurricanes.

Microwave radiometer measurements represent an alternative data source for addressing the confusing state of modeling C_{10} and W_c. The stepped frequency microwave radiometer (SFMR) measures BTs of the ocean surface at six *C*-band microwave channels [44] and it has been used to obtain TC rain rate and wind speed for decades by now [45], [46]. A recent comprehensive analysis of several hundred sets of SFMR measurements from hurricane reconnaissance and research missions [47] is employed for examining different formulas of the drag coefficient and whitecap coverage [48]. The analysis demonstrates that microwave radiometer data are useful for evaluating C_{10} and W_c formulas. The optimal C_{10} and W_c functions determined from the study are

$$C_{10} = \begin{cases} 10^{-4}\left(-0.0160U_{10}^2 \right. \\ \quad \left. +0.967U_{10} + 8.058\right), & U_{10} \le 35 \text{ m/s} \\ 2.23 \times 10^{-3}(U_{10}/35)^{-1}, & U_{10} > 35 \text{ m/s} \end{cases} \tag{3}$$

$$W_c = \begin{cases} 0, & u_* \le 0.11 \text{ m/s} \\ 0.30(u_* - 0.11)^3, & 0.11 < u_* \le 0.40 \text{ m/s} \\ 0.07u_*^{2.5}, & u_* > 0.40 \text{ m/s} \end{cases}. \tag{4}$$

These optimal C_{10} and W_c functions are used in all the microwave computations presented in the rest of this article.

III. Discussion

A. Feedback to Microwave Emission Computation

The validity of (3) and (4) is further evaluated with additional microwave radiometer datasets [49]–[57], as detailed in [58]–[60]. As mentioned earlier, the H2018 wave spectrum model incorporates the updated C_{10} function and revision of cmDm waves derived from GNSSR LPMSS analysis. The first application of the H2018 model is documented in [58] for microwave radiometer BT computation. These studies [58]–[60] summarize the results of analyzing a wide range of microwave radiometer data sources of both horizontal and vertical polarizations, with frequency ranging from 1 to 37 GHz, earth incidence angle (EIA) from 0° to 65°, and wind speed extending to more than 90 m/s. The data sources include the following:

SFMR (to ∼70 m/s, 4.7 to 7.2 GHz, 0° EIA);
WindSat (to ∼43 m/s, 6.8, 10.7, 18.7, 23.8, and 37.0 GHz, 49° to 54° EIA);
Soil moisture active passive (SMAP) (to ∼90 m/s, 1.4 GHz, 40° EIA); and
Soil moisture and ocean salinity (SMOS) (to ∼44 m/s, 1.4 GHz, 10° to 65° EIA).
The analytical SSA/SPM solutions are in excellent agreement with all the assembled microwave radiometer measurements.

B. Improvement in VV NRCS Computation

Fig. 1 compares the computed VV NRCS (σ_{0VV}) for *Ku*-, *C*-, and *L*-band using H2018 and H2015, showing general and consistent improvements in the results using H2018 for all frequencies in comparison to those using H2015. The *L*-band GMF shown in Fig. 1(c) is from the SMAP analyses [49], [50], the applicable maximum wind speed extends further to 50 m/s, the incidence angle range is from 35° to 45°. With H2018 (black

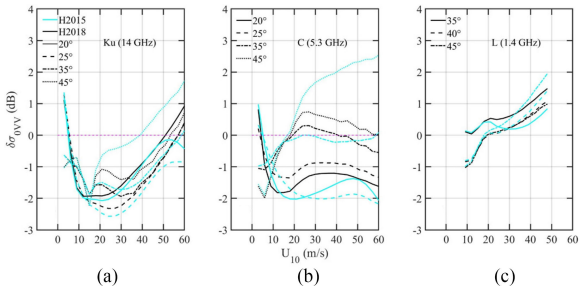

Fig. 1. Difference between GMFs and SSA2 solutions of VV NRCS. (a) *Ku*-band (14 GHz). (b) *C*-band (5.3 GHz). (c) *L*-band (1.4 GHz). The cyan curves are results computed with H2015 spectrum model and black curves are results with the H2018 model.

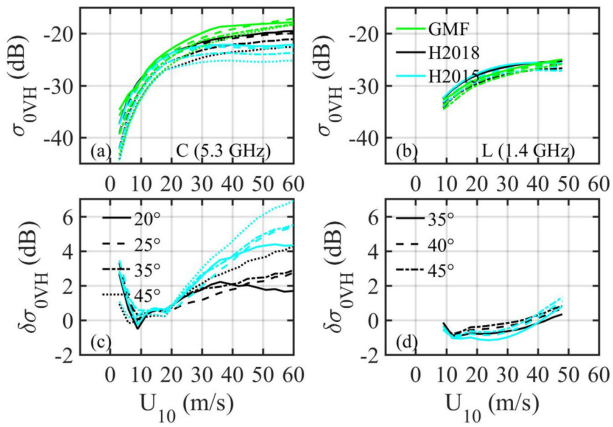

Fig. 2. Top: VH GMFs and SSA2 solutions. (a) *C*-band (5.3 GHz). (b) *L*-band (1.4 GHz). Green curves are GMFs; cyan curves are SSA2 solutions with the H2015 roughness model; black curves are SSA2 solutions with the H2018 model. Bottom: Difference between GMFs and SSA2 solutions. (c) *C*-band (5.3 GHz). (d) *L*-band (1.4 GHz). The *C*-band GMF is from Sentinel-1 analysis [62], the *L*-band GMF is from SMAP analysis [49], [50].

curves), the differences between GMFs and computations are as follows:

Ku-band (within -2.2 and $+1.2$ dB for $U_{10} \leq 60$ m/s and θ between 20° and 45°),

C-band (within -1.8 and $+0.8$ dB for $U_{10} \leq 60$ m/s and θ between 20° and 45°), and

L-band (within -1.0 and $+1.4$ dB for $U_{10} \leq 50$ m/s and θ between 35° and 45°).

C. EM Model Results Incorporating Updated Ocean Surface Properties

With the updated information on the drag coefficient, surface roughness, and whitecap coverage implemented in the EM scattering and emission models, there are considerable improvement in the computed NRCS and excess emissivity. Good agreements between computed VV NRCSs and field data represented by the *L*-, *C*-, and *Ku*-band GMFs are achieved over a wide wind speed range: the maximum wind speeds for the three frequencies in the comparison study are 50, 60, and 60 m/s, respectively. Excellent agreements are also found in comparing the SSA/SPM EM solutions with microwave radiometer data of WindSat (6.8–37 GHz), SFMR (4.7–7.2 GHz), and *L*-band SMAP and SMOS (1.4 GHz): the maximum wind speeds for the three data groups are about 43, 53, and 90 m/s [59]. The correlation coefficients of model-measurement comparisons are all better than 0.97 for both active and passive microwave sensors. These comparison results of field measurements with active and passive microwave computations offer confidence on the robustness of the recent development in modeling the drag coefficient, whitecap coverage, and surface roughness discussed in Section II.

D. Application to Cross-Polarization Backscattering

There is considerable interest in clarifying the cross-polarization backscattering VH from the ocean surface in support of the planned incorporation of cross-polarization channel in the next generation microwave scatterometers [61]. Fig. 2 shows the GMFs and SSA2 solutions of VH NRCS and their differences for *C*- and *L*-band based on H2015 and H2018 surface roughness spectrum models (no *Ku*-band VH GMF has been reported yet). The *C*-band GMF (MS1A) used here is from the analysis of Sentinel-1 data [62], the *L*-band GMF is from the SMAP analysis [49], [50].

For the *L*-band results shown in the right column [see Fig. 2(b) and (d)], the agreement between GMF and SSA2 solutions is mostly within about ±1.2 dB for H2015, and the H2018 roughness spectrum yields further improvement to within ±0.8 dB. The level of agreement is similar to the VV NRCS [see Fig. 1(c)]. The outcome indicates that surface scattering dominates both VV and VH in *L*-band. The SSA2 solutions, which account for the first- and second-order Bragg scattering, are sufficient to explain the available observations ($U_{10} \leq 50$ m/s and θ between 35° and 45°) to within ±1 dB. The importance of incorporating the second-order Bragg scattering in the VH computation was pointed out almost a decade ago by Voronovich and Zavorotny [63], [64].

For *C*-band VH difference [see Fig. 2(c)], considerable improvement is found in the solutions computed with the H2018 roughness spectrum compared to those with the H2015 spectrum. The improvement increases from 1 dB at wind speed about 25 m/s to 3 dB at 60 m/s. Overall, the agreement between GMF and SSA2 solutions using the H2018 spectrum is within ±2 dB except for $\theta = 45°$ and $U_{10} > \sim 30$ m/s, for which the difference can grow to about 4 dB at 60 m/s. This level of agreement is slightly worse than that of the VV comparison [see Fig. 2(b)].

The VV and VH results with the H2018 spectrum for *L*- and *C*-band are summarized in the following:

VV:

L-band (within -1.0 and $+1.4$ dB for $U_{10} < 50$ m/s and θ between 35° and 45°),

C-band (within -1.8 and $+0.8$ dB for $U_{10} < 60$ m/s and θ between 20° and 45°)

VH:

L-band (within -0.8 and $+0.8$ dB for $U_{10} < 50$ m/s and θ between 35° and 45°),

C-band (within -0.2 and $+2.6$ dB for $U_{10} < 60$ m/s and θ between 20° and 45°, except for 45° and $U_{10} > \sim 30$ m/s).

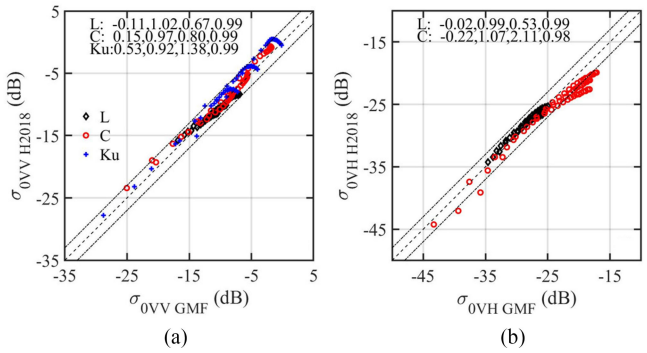

Fig. 3. Examples of comparing GMFs with computed NRCSs using the H2018 spectrum. (a) *L*-, *C*-, and *Ku*-band VV, and (b) *L*- and *C*-band VH. The statistics printed on the upper edge of each panel are bias, slope of linear regression, RMS difference, and correlation coefficient.

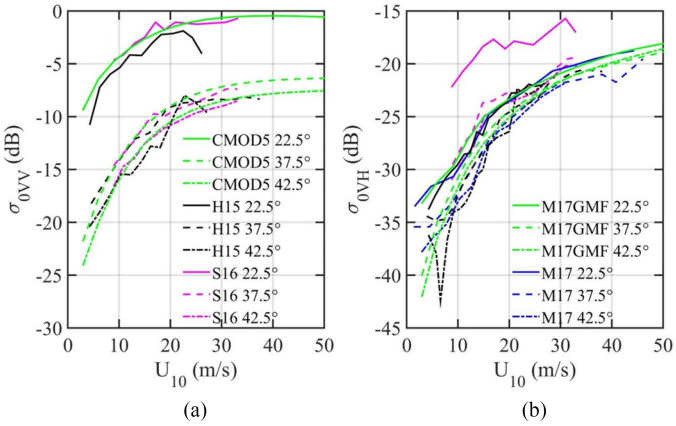

Fig. 4. Examples of microwave NRCS reported in 2015 (H15, black curves) [65], 2016 (S16, magenta curves) [66] and 2017 (M17, green curves*) [62] at three incidence angles. (a) VV. (b) VH. * M17 did not present VV, the green curves in (a) are CMOD5.

Fig. 3 presents the results in scatter plots comparing the modeled NRCS and field data represented by the GMFs (*L*-, *C*-, and *Ku*-band for VV, and *L*- and *C*-band for VH). The maximum wind speeds for the *L*-, *C*-, and *Ku*-band are 50, 60, and 60 m/s, respectively. The two dashed-dotted lines show the ± 2 dB envelops. The regression statistics [bias, slope of linear regression, root mean square (RMS) difference, and correlation coefficient] printed at the upper edge of the figure show good agreement between computation and measurement. The VV NRCSs are most useful for examining the surface roughness spectrum because of the dominance by Bragg scattering.

E. Measurement Issues

The VH GMF is still evolving, especially for the *C*-band. One of the main reasons is that the reported VH data from different sources do not always agree with each other. For example, Fig. 3 shows the NRCS reported in 2015 (H15) [65], 2016 (S16) [66], and 2017 (M17) [62] at three incidence angles. The data used in the three studies are from RadarSat-2, airborne imaging wind and rain airborne profiler, and Sentinel-1A, respectively. Both H15 and S16 report VV and VH, M17 focuses on VH to establish a new GMF (MS1A). The GMFs superimposed with green curves in the figure are CMOD5 for VV and MS1A for VH. The agreement in the VV data from different sources is reasonably good [see Fig. 4(a)] but the S16 VH data are obviously much higher than the remaining two sources [see Fig. 4(b)].

Two major issues are highlighted here: polarization mixing and signal noise; both problems are caused by the relatively weak signal of the VH sea return. These issues have caused considerable differences in the reported VH dependence on wind speed, as illustrated in Fig. 4(b). The polarization mixing is especially significant for airborne data processing due to the aircraft pitch angle [67].

The airborne results reported in 2016 [66] and 2018 [67] are given in Fig. 5(a) and (b). The latter has implemented a polarization mixing correction procedure that decreases the VH signal by as much as 6 dB over a wide range of wind speed and incidence angle; in the figure, smooth curves are the 2016 results and markers with error bars are the 2018 results.

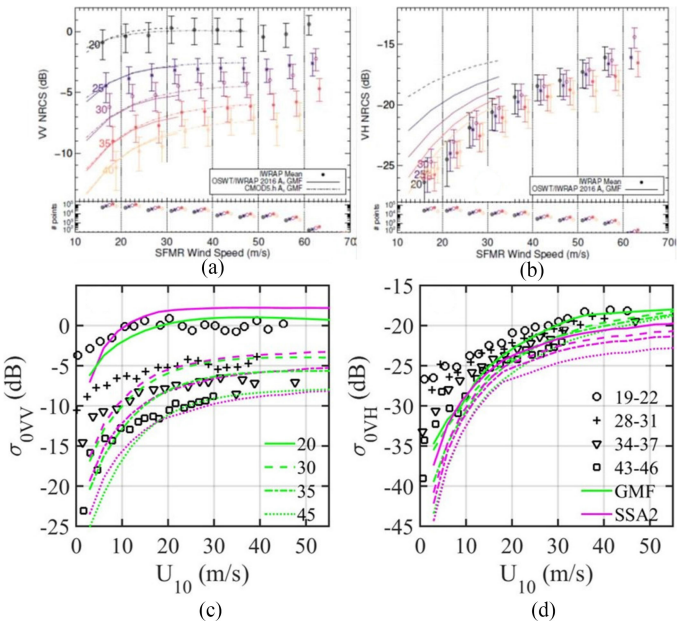

Fig. 5. Top: Airborne *C*-band NRCS reported in 2016 [66] and 2018 [67]. (a) VV. (b) VH, (reproducing [67, Figs. 1 and 3]). The upper panels show five sets of averages, each over 2° of incidence angle, the lower panel show the number of samples. Each set shifts slightly for clarity. The markers with error bars are the 2018 results, and the smooth curves are the 2016 results, notice the large difference in the VH data. Bottom: Sentinel-1A data reported in 2017 (VH only) [62] and 2018 (VV and VH) [68]. (c) VV. (d) VH. The MS1A GMF (green curves) represent the 2017 VH results in (d) and markers are the 2018 results. For reference, magenta curves show the SSA2 solutions. Green curves in (c) are the CMOD5 VV GMF.

Satellite data reported in different years also show differences of similarly large magnitude. For example, Fig. 5(c) and (d) are the Sentinel-1A results reported in 2017 [62] and 2018 [68]. The 2018 study presents scatter plots of VV and VH versus the SMAP wind-induced excess BT ΔT_b. Here, markers show the 2018 results, with ΔT_b converted to the surface wind speed [59]. The MS1A GMF represents the 2017 VH results. There are obvious and significant differences in the VH NRCS

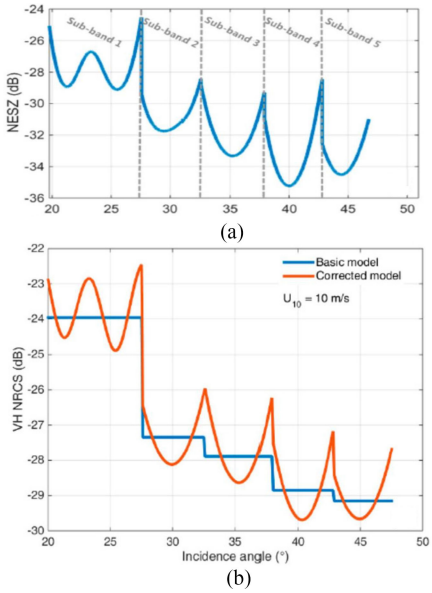

Fig. 6. (a) Sentinel-1A NESZ for sub-bands 1–5. (b) VH NRCS at 10 m/s with two different noise treatments; (reproducing [69, Figs. 1 and 11]).

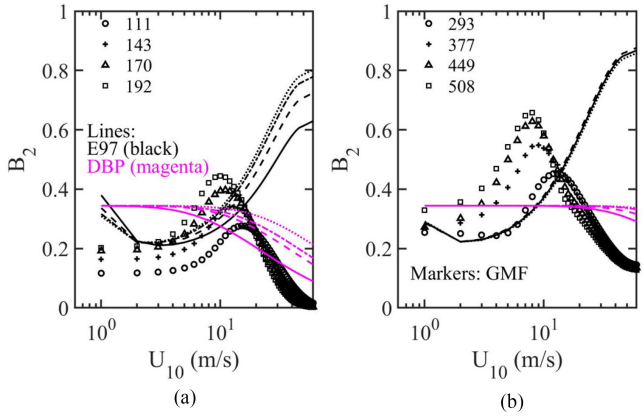

Fig. 7. Comparison of the directional distribution coefficient B_2 based on the E97 and DBP models with those obtained from (a) CMOD5.n GMF and (b) Ku2001 GMF. The incidence angles used in the computation are 20°, 30°, 40°, and 50°. The corresponding Bragg wave numbers are illustrated in the legends.

reported in 2017 and 2018 over a wide range of wind speed and incidence angle [see Fig. 5(d)].

For reference, magenta curves in Fig. 5(c) and (d) show the SSA2 VV and VH solutions. As noted earlier, the *C*-band difference between SSA2 solutions and GMFs is within about ±2 dB for VV and about ±2.6 dB for VH in the range of wind speed (0–54 m/s) and incidence angle (20°–45°) illustrated here. Except for VH in high winds greater than about 25 m/s, the differences between measurements (markers) and GMFs are larger than those between the SSA2 solutions and GMFs [see Fig. 5(c) and (d)].

The noise level of microwave sensors presents another problem for processing the VH ocean returns. TC monitoring prefers wide swatch. The extra-wide swath mode of Sentinel-1A (up to 410 km wide) covers incidence angles from about 18.9° to 47.0°. It combines five sub-bands in the range direction [69]. Fig. 6(a), reproducing [69, Fig. 1], shows the noise equivalent sigma zero (NESZ), which has a complicated incidence angle dependence that also varies in different sub-bands. The noise level is comparable to the expected VH NRCS in low and moderate wind speeds, e.g., see Figs. 4(b) and 5(d). The noise removal during data processing becomes a source of uncertainty. Fig. 6(b), reproducing [69, Fig. 11], is an example of the VH NRCS at 10 m/s wind speed resulting from denoising processing with their basic model and corrected model: the difference within a narrow incidence angle range around 27° is about 4 dB. Because of its small magnitude, the denoising is an important and a difficult step for VH data processing. A detailed study of noise removal procedure is described in [70].

F. Other Issues

In this study, the VV NRCS of ocean surface backscattering has been used to expand the cmDm wave database. The HH NRCS is not employed although its magnitude is much closer to VV in comparison with VH. It is well known that the HH scattering involves more than tilting and Bragg resonance mechanisms, as demonstrated in [71, Figs. 6 and 7] with the tilted Bragg computation, and in [17, Figs. 3, 8, and 10] with the SSA2 computation. The agreement between computed HH solutions and measurements starts to deteriorate at incidence angle greater than about 35°. Wave breaking has been suggested to be a main missing mechanism, e.g., [8], [72]–[75], but it remains uncertain regarding how to account for the wave breaking contribution in microwave scattering.

In addition to wave breaking contribution, directional distribution is another subject that remains unsettled. Two of the most frequently employed directional distribution functions are the Elfouhaily *et al.* (the E97 function) [7], and Donelan–Banner–Plant (the DBP function) [76]–[79]. However, the fidelity of either directional distribution is questionable. An example is shown in [17, Fig. 1] illustrating the disagreement between the E97 function and the CMOD5.n and Ku2001 GMFs. Fig. 7 reproduces [17, Fig. 1] together with the DBP results superimposed, showing similar level of disagreement between the DBP directional distribution and the GMFs. The DBP directional function is used in this article with the understanding that neither directional function is satisfactory. The results computed with the E97 function is slightly worse as evaluated from agreement between computed solutions and the GMFs. There are continuous efforts intending to improve the directional distribution function of cmDm waves, e.g., [80]–[87], but the progress is rather slow.

IV. Summary

Surface waves represent the ocean surface roughness, which influences emission and scattering of EM waves at the air-sea interface. In moderate to high winds, air entrained by wave breaking modifies the dielectric properties of the surface layer. Surface wind stress drives both surface roughness and wave

breaking (whitecaps). With wind speed as the input oceanographic/atmospheric parameter, the magnitude of surface wind stress varies with the chosen drag coefficient formula. Consequently, for the same wind speed the input roughness spectrum and whitecap coverage for EM computation may differ from selecting different drag coefficient formulas.

Microwave signals from the ocean surface contain the key information of ocean surface roughness, whitecap coverage, and drag coefficient. Refinement of surface roughness spectrum has taken advantage of the property that Bragg resonance mechanism dominates VV backscattering. The development of surface roughness model has included in its cmDm wave database the spectral information derive from global scatterometer VV NRCSs and GNSSR LPMSSs. For the drag coefficient and whitecap coverage, the effort to improve their formulations makes use of the extensive microwave radiometer data collected in TCs. The analysis shows that $C_{10} \sim U_{10}^{-1}$, $u_* \sim U_{10}^{0.5}$, and $W_c \sim U_{10}^{1.25}$ in very high winds (U_{10} greater than about 35 m/s).

These recent improvements of drag coefficient, whitecap coverage, and surface roughness are incorporated in microwave emission and scattering models. The emission computations yield excellent agreement with global data covering a wide range of frequency, incidence angle, wind speed, and both vertical and horizontal polarizations. The backscattering computations are also in good agreement with scatterometer GMFs [see Figs. (1)–(3)]. For *L*-band, the difference between analytical solutions and GMFs is within about 1 dB for both VV and VH in wind speed below 50 m/s and incidence angle between 35° and 45°. For *Ku*- and *C*-band VV, the difference is within about ± 2 dB in wind speed below 60 m/s and incidence angle between 20° and 45°, for *C*-band *VH*, the difference is within about ± 2.6 dB for the same wind speed and incidence angle ranges (*Ku*-band VH GMF has not been reported). The difference between analytical VH solutions and GMFs is similar to or generally better than the difference between reported VH NRCS measurements and GMFs or data uncertainties [see Figs. (4)–(6)].

ACKNOWLEDGEMENT

The author is grateful for the comments and suggestions from three anonymous reviewers. This is U.S. Naval Research Laboratory Publication JA/7260—19-0465.

REFERENCES

[1] W. J. Pierson and R. A. Stacy, "The elevation slope and curvature spectra of a wind roughened sea surface," NASA, Washington, DC, USA, Contract Rep. CR-2247, 1973.

[2] A. W. Bjerkaas and F. W. Riedel, "Proposed model for the elevation spectrum of a wind-roughened sea surface," , Appl. Phys. Lab., Johns Hopkins Univ., Laurel, MD, USA, Tech. Memo TG 1328, 1979.

[3] A. K. Fung and K. K. Lee, "A semi-empirical sea-spectrum model for scattering coefficient estimation," *IEEE J. Ocean. Eng.*, vol. OE-7, no. 4, pp. 166–176, Oct. 1982.

[4] S. L. Durden and J. F. Vesecky, "A physical radar cross-section model for a wind-driven sea with swell," *IEEE J. Ocean. Eng.*, vol. OE-10, no. 4, pp. 445–451, Oct. 1985.

[5] M. A. Donelan and W. J. Pierson, "Radar scattering and equilibrium ranges in wind-generated waves with application to scatterometry," *J. Geophys. Res.*, vol. 92, pp. 4971–5029, May 1987.

[6] J. R. Apel, "An improved model of the ocean surface wave vector spectrum and its effects on radar backscatter," *J. Geophys. Res.*, vol. 99, pp. 16269–16291, Aug. 1994.

[7] T. Elfouhaily, B. Chapron, K. Katsaros, and D. Vandemark, "A unified directional spectrum for long and short wind-driven waves," *J. Geophys. Res.*, vol. 102, no. C7, pp. 15781–15796, Jul. 1997.

[8] V. Kudryavtsev, V. Makin, and B. Chapron, "Coupled sea surface atmosphere model, 2, Spectrum of short wind waves," *J. Geophys. Res.*, vol. 104, no. C4, pp. 7625–7639, Apr. 1999.

[9] P. A. Hwang, "Wave number spectrum and mean-square slope of intermediate-scale ocean surface waves," *J. Geophys. Res.*, vol. 110, Oct. 2005, Art. no. C10029.

[10] P. A. Hwang and D. W. Wang, "An empirical investigation of source term balance of small scale surface waves," *Geophys. Res. Lett.*, vol. 31, no. 8, Aug. 2004, Art. no. L15301.

[11] P. A. Hwang, "Observations of swell influence on ocean surface roughness," *J. Geophys. Res.*, vol. 113, Dec. 2008, Art. no. C12024.

[12] F. J. Wentz and D. K. Smith, "A model function for the ocean-normalized radar cross section at 14 GHz derived from NSCAT observations," *J. Geophys. Res.*, vol. 104, no. C5, pp. 11499–11514, May 1999.

[13] H. Hersbach, A. Stoffelen, and S. de Haan, "An improved C-band scatterometer ocean geophysical model function: CMOD5," *J. Geophys. Res.*, vol. 112, Mar. 2007, Art. no. C03006.

[14] O. Isoguchi and M. Shimada, "An L-band ocean geophysical model function derived from PALSAR," *IEEE Trans. Geosci. Remote Sens.*, vol. 47, no. 7, pp. 1925–1936, Jul. 2009.

[15] S. H. Yueh, S. J. Dinardo, A. G. Fore, and F. K. Li, "Passive and active L-band microwave observations and modeling of ocean surface winds," *IEEE Trans. Geosci. Remote Sens.*, vol. 48, no. 8, pp. 3087–3100, Aug. 2010.

[16] P. A. Hwang, D. M. Burrage, D. W. Wang, and J. C. Wesson, "Ocean surface roughness spectrum in high wind condition for microwave backscatter and emission computations," *J. Atmos. Ocean. Tech.*, vol. 30, no. 9, pp. 2168–2188, Sep. 2013.

[17] P. A. Hwang and F. Fois, "Surface roughness and breaking wave properties retrieved from polarimetric microwave radar backscattering," *J. Geophys. Res.*, vol. 120, no. 5, pp. 3640–3657, May 2015.

[18] P. A. Hwang, "A study of the wavenumber spectra of short water waves in the ocean. Part 2: Spectral model and mean square slope," *J. Atmos. Ocean. Tech.*, vol. 14, no. 10, pp. 1174–1186, Oct. 1997.

[19] Y. G. Trokhimovski and V. G. Irisov, "The analysis of wind exponents retrieved from microwave radar and radiometric measurements," *IEEE Trans. Geosci. Remote Sens.*, vol. 38, no. 1, pp. 470–479, Jan. 2000.

[20] T. Meissner, L. Ricciardulli, and F. Wentz, "The emission and scattering of L-band microwave radiation from rough ocean surfaces and wind speed measurements from the Aquarius sensor," *J. Geophys. Res. Ocean.*, vol. 119, pp. 6499–6522, Sep. 2014.

[21] S. J. Katzberg and J. Dunion, "Comparison of reflected GPS wind speed retrievals with dropsondes in tropical cyclones," *Geophys. Res. Lett.*, vol. 36, Sep. 2009, Art. no. L17602.

[22] S. J. Katzberg, J. Dunion, and G. G. Ganoe, "The use of reflected GPS signals to retrieve ocean surface wind speeds in tropical cyclones," *Radio Sci.*, vol. 48, pp. 371–387, Jul. 2013.

[23] S. Gleason, "Space based GNSS scatterometry: Ocean wind sensing using empirically calibrated model," *IEEE Trans. Geosci. Remote Sens.*, vol. 51, no. 9, pp. 4853–4863, Sep. 2013.

[24] S. Gleason *et al.*, "Study of surface wind and mean square slope correlation in hurricane Ike with multiple sensors," *IEEE J. Sel. Topics Appl. Earth Observ. Remote Sens.*, vol. 11, no. 6, pp. 1975–1988, Jun. 2018.

[25] P. A. Hwang, Y. Fan, F. J. Ocampo-Torres, and H. García-Nava, "Ocean surface wave spectra inside tropical cyclones," *J. Phys. Oceanogr.*, vol. 47, no. 10, pp. 2293–2417, Oct. 2017.

[26] P. A. Hwang and Y. Fan, "Low-frequency mean square slopes and dominant wave spectral properties: Toward tropical cyclone remote sensing," *IEEE Trans. Geosci. Remote Sens.*, vol. 56, no. 12, pp. 7359–7368, Dec. 2018.

[27] F. Felizardo and W. K. Melville, "Correlations between ambient noise and the ocean surface wave field," *J. Phys. Oceanogr.*, vol. 25, no. 4, pp. 513–532, Apr. 1995.

[28] M. D. Powell, P. J. Vickery, and T. A. Reinhold, "Reduced drag coefficient for high wind speeds in tropical cyclones," *Nature*, vol. 422, pp. 279–283, Mar. 2003.

[29] E. Jarosz, D. A. Mitchell, D. W. Wang, and W. J. Teague, "Bottom-up determination of air-sea momentum exchange under a major tropical cyclone," *Science*, vol. 315, pp. 1707–1709, Mar. 2007.

[30] L. H. Holthuijsen, M. D. Powell, and J. D. Pietrzak, "Wind and waves in extreme hurricanes," *J. Geophys. Res.*, vol. 117, no. C09, Sep. 2012, Art. no. C09003.

[31] M. D. Powell, "Drag coefficient distribution and wind speed dependence in tropical cyclones," Final Report to the NOAA JHT Program, Atlantic Oceanographic and Meteorological Laboratory, Rep., Miami, Florida, Rep. JH107, 2006.

[32] M. M. Bell, M. T. Montgomery, and K. A. Emanuel, "Air-sea enthalpy and momentum exchange at major hurricane wind speeds observed during CBLAST," *J. Atmos. Sci.*, vol. 69, no. 11, pp. 3197–3122, Nov. 2012.

[33] E. C. Monahan, "Oceanic whitecaps," *J. Phys. Oceanogr.*, vol. 1, pp. 139–144, Apr. 1971.

[34] Y. Toba and M. Chaen, "Quantitative expression of the breaking of wind waves on the sea surface," *Records Oceanogr. Works Japan*, vol. 12, no. 1, pp. 1–11, Mar. 1973.

[35] D. B. Ross and V. Cardone, "Observations of oceanic whitecaps and their relation to remote measurements of surface wind stress," *J. Geophys. Res.*, vol. 79, no. 3, pp. 444–452, Jan. 1974.

[36] D. Xu, X. Liu, and D. Yu, "Probability of wave breaking and whitecap coverage in a fetch-limited sea," *J. Geophys. Res.*, vol. 105, no. C6, pp. 14253–14259, Jun. 2000.

[37] C. Lafon, J. Piazzola, P. Forget, O. Le Calve, and S. Despiau, "Analysis of the variations of the whitecap fraction as measured in a coastal zone," *Bound.-Layer Meteorol.*, vol. 111, pp. 339–360, 2004.

[38] C. Lafon, J. Piazzola, P. Forget, and S. Despiau, "Whitecap coverage in coastal environment for steady and unsteady wave field conditions," *J. Mar. Syst.*, vol. 66, pp. 38–46, Oct. 2007.

[39] Y. Sugihara, H. Tsumori, T. Ohga, H. Yoshioka, and S. Serizawa, "Variation of whitecap coverage with wave-field conditions," *J. Mar. Syst.*, vol. 66, pp. 47–60, Oct. 2007.

[40] A. H. Callaghan, G. de Leeuw, L. H. Cohen, and C. D. O'Dowd, "The relationship of oceanic whitecap coverage to wind speed and wind history," *Geophys. Res. Lett.*, vol. 35, Dec. 2008, Art. no. L23609.

[41] S. E. Brumer *et al.*, "Whitecap coverage dependence on wind and wave statistics as observed during SO GasEx and HiWinGS," *J. Phys. Oceanogr.*, vol. 47, no. 9, pp. 2211–2235, Sep. 2017.

[42] P. A. Hwang and M. A. Sletten, "Energy dissipation of wind-generated waves and whitecap coverage," *J. Geophys. Res.*, vol. 113, Feb. 2008, Art. no. C02012.

[43] P. A. Hwang, "Foam and roughness effects on passive microwave remote sensing of the ocean," *IEEE Trans. Geosci. Remote Sens.*, vol. 50, no. 8, pp. 2978–2985, Aug. 2012.

[44] C. T. Swift, D. C. DeHority, P. G. Black, and J.-Z. Chein, "Microwave remote sensing of ocean surface wind speed and rain rates over tropical storms," in *Proc. Frontiers Remote Sens. Oceans Troposphere Air Space Platforms: Proc. URSI Commission F Symp. Workshop, NASA Conf. Pub.*, 1984, vol. 2303, pp. 281–286.

[45] E. W. Uhlhorn and P. G. Black, "Verification of remotely sensed sea surface winds in hurricanes," *J. Atmos. Ocean. Technol.*, vol. 20, no. 1, pp. 99–116, Jan. 2, 2003.

[46] E. W. Uhlhorn, P. G. Black, J. L. Franklin, M. Goodberlet, J. Carswell, and A. S. Goldstein, "Hurricane surface wind measurements from an operational stepped frequency microwave radiometer," *Mon. Wea. Rev.*, vol. 135, pp. 3070–3085, Sep. 2007.

[47] B. W. Klotz and E. W. Uhlhorn, "Improved stepped frequency microwave radiometer tropical cyclone surface winds in heavy precipitation," *J. Atmos. Ocean. Technol.*, vol. 31, no. 11, pp. 2392–2408, Nov. 2014.

[48] P. A. Hwang, "High wind drag coefficient and whitecap coverage derived from microwave radiometer observations in tropical cyclones," *J. Phys. Oceanogr.*, vol. 48, no. 10, pp. 2221–2232, Oct. 2018.

[49] S. H. Yueh *et al.*, "SMAP L-band passive microwave observations of ocean surface wind during severe storms," *IEEE Trans. Geosci. Remote Sens.*, vol. 54, no. 12, pp. 7339–7350, Dec. 2016.

[50] A. G. Fore, S. H. Yueh, B. W. Stiles, W. Tang and A. K. Hayashi, "On extreme winds at L-Band with the SMAP synthetic aperture radar," *Remote Sens.*, vol. 11, no. 1–7, May 2019, Art. no. 1093.

[51] P. A. Hwang and Y. Fan, "Effective fetch and duration of tropical cyclone wind fields estimated from simultaneous wind and wave measurements: Surface wave and air-sea exchange computation," *J. Phys. Oceanogr.*, vol. 47, no. 2, pp. 447–470, Feb. 2017.

[52] J. W. Sapp, S. O. Alsweiss, A. Jelenak, P. S. Chang, and J. Carswell, "Stepped frequency microwave radiometer wind-speed retrieval improvements," *Remote Sens.*, vol. 11, no. 3, Jan. 2019, Art. no. 214.

[53] T. Meissner and F. J. Wentz, "Wind-vector retrievals under rain with passive satellite microwave radiometers," *IEEE Trans. Geosci. Remote Sens.*, vol. 47, no. 9, pp. 3065–3083, Sep. 2009.

[54] N. Reul, J. Tenerelli, B. Chapron, D. Vandemark, Y. Quilfen, and Y. Kerr, "SMOS satellite L-band radiometer: A new capability for ocean surface remote sensing in hurricanes," *J. Geophys. Res.*, vol. 117, Feb. 2012, Art. no. C02006.

[55] S. H. Yueh *et al.*, "L-band passive and active microwave geophysical model functions of ocean surface winds and applications to Aquarius retrieval," *IEEE Trans. Geosci. Remote Sens.*, vol. 51, no. 9, pp. 4619–4632, Sep. 2013.

[56] N. Reul *et al.*, "A revised L-band radio-brightness sensitivity to extreme winds under tropical cyclones: The five year SMOS-storm database," *Remote Sens. Environ.*, vol. 180, pp. 274–291, Apr. 2016.

[57] T. Meissner, L. Ricciardulli, and F. Wentz, "Capability of the SMAP mission to measure ocean surface winds in storms," *Bull. Amer. Meteorol. Soc.*, vol. 98, pp. 1660–1677, Aug. 2017.

[58] P. A. Hwang, "Surface foam and L-band microwave radiometer measurements in high winds," *IEEE Trans. Geosci. Remote Sens.*, vol. 57, no. 5, pp. 2766–2776, May 2019.

[59] P. A. Hwang, N. Reul, T. Meissner, and S. H. Yueh, "Ocean surface foam and microwave emission: Dependence on frequency and incidence angle," *IEEE Trans. Geosci. Remote Sens.*, vol. 57, no. 10, pp. 8223–8234, Oct. 2019.

[60] P. A. Hwang, N. Reul, T. Meissner, and S. H. Yueh, "Whitecap and wind stress observations by microwave radiometers: Global coverage and extreme conditions," *J. Phys. Oceanogr.*, vol. 49, pp. 2291–2307, 2019.

[61] F. Fois, P. Hoogeboom, F. Le Chevalier, and Ad Stoffelen, "Future ocean scatterometry: On the use of cross-polar scattering to observe very high winds," *IEEE Trans. Geosci. Remote Sens.*, vol. 53, no. 9, pp. 5009–5020, Sep. 2015.

[62] A. A. Mouche, B. Chapron, B. Zhang, and R. Husson, "Combined co- and cross-polarized SAR measurements under extreme wind conditions," *IEEE Trans. Geosci. Remote Sens.*, vol. 47, no. 12, pp. 3065–3083, Dec. 2017.

[63] A. G. Voronovich and V. U. Zavorotny, "Depolarization of microwave backscattering from a rough sea surface: Modeling with small-slope approximation," in *Proc. Int. Symp. Geosci. Remote Sens.*, Jul. 2011, pp. 2003–2036.

[64] A. G. Voronovich and V. U. Zavorotny, "Full-polarization modeling of monostatic and bistatic radar scattering from a rough sea surface," *IEEE Trans. Antennas Propag.*, vol. 62, no. 3, pp. 1363–1371, Mar. 2014.

[65] P. A. Hwang *et al.*, "Cross polarization geophysical model function for C-band radar backscattering from the ocean surface and wind speed retrieval," *J. Geophys. Res.*, vol. 120, no. C2, pp. 893–909, Feb. 2015.

[66] J. W. Sapp, S. O. Alsweiss, Z. Jelenak, P. S. Chang, S. J. Frasier, and J. C. Carswell, "Airborne co-polarization and cross-polarization observations of the ocean-surface NRCS at C-band," *IEEE Trans. Geosci. Remote Sens.*, vol. 54, no. 10, pp. 5975–5992, Oct. 2016.

[67] J. Sapp, Z. Jelenak, P. Chang, and S. Frasier, "C-band cross-polarization ocean surface observations in hurricane Matthew," in *Proc. Int. Geosci. Remote Sens. Symp.*, Jul. 2018, pp. 5595–5598.

[68] Y. Zhao, A. Mouche, B. Chapron, and N. Reul, "Direct comparison between active C-band radar and passive L-Band radiometer measurements: Extreme event cases," *IEEE Geosci. Remote Sens. Lett.*, vol. 15, no. 6, pp. 897–901, Jun. 2018.

[69] Y. Gao, C. Guan, J. Sun, and L. Xie, "A wind speed retrieval model for Sentinel-1A EW mode cross-polarization images," *Remote Sens.*, vol. 11, no. 2, Jan. 2019, Art. no. 153.

[70] J.-W. Park, A. A. Korosov, M. Babiker, S. Sandven, and J.-S. Won, "Efficient thermal noise removal for sentinel-1 TOPSAR cross-polarization channel," *IEEE Trans. Geosci. Remote Sens.*, vol. 56, no. 3, pp. 1555–1565, Mar. 2018.

[71] G. R. Valenzuela, "Theories for the interaction of electromagnetic and oceanic waves—A review," *Bound.-Layer Meteorol.*, vol. 13, no. 1–4, pp. 61–85, Jan. 1978.

[72] L. B. Wetzel, "Electromagnetic scattering from the sea at low grazing angles," in *Surface Waves and Fluxes. Vol. II – Remote Sensing*, G. L. Geernaert and W. J. Plant Eds. Dordrecht, The Netherlands: Kluwer Academic Publ., pp. 109–171, 2009.

[73] D. B. Trizna, "A model for Brewster angle damping and multipath effects on the microwave radar sea echo at low grazing angles," *IEEE Trans. Geosci. Remote Sens.*, vol. 35, no. 5, pp. 1232–1244, Sep. 1997.

[74] J. Li, M. Zhang, W. Fan, and D. Nie, "Facet-based investigation on microwave backscattering from sea surface with breaking waves: Sea spikes and SAR imaging," *IEEE Trans. Geosci. Remote Sens.*, vol. 55, no. 4, pp. 2313–2325, Apr. 2017.

[75] V. N. Kudryavtsev, S. Fan, B. Zhang, A. A. Mouche, and B. Chapron, "On quad-polarized SAR measurements of the ocean surface," *IEEE Trans. Geosci. Remote Sens.*, vol. 57, no. 11, pp. 8362–8370, Nov. 2019.
[76] M. A. Donelan, J. Hamilton, and W. H. Hui, "Directional spectra of wind-generated waves," *Phil. Trans. Roy. Soc. Lond.*, vol. A315, pp. 509–562. 1985.
[77] M. A. Donelan and W. J. Pierson, "Radar scattering and equilibrium ranges in wind-generated waves with application to scatterometry," *J. Geophys. Res.*, vol. 92, pp. 4971–5029, May 1987.
[78] M. L. Banner, "Equilibrium spectra of wind waves," *J. Phys. Oceanogr.*, vol. 20, no. 7, pp. 966–984, Jul. 1990.
[79] W. J. Plant, "A stochastic, multiscale model of microwave backscatter from the ocean," *J. Geophys. Res.*, vol. 107, no. C9, Sep. 2002, Art. no. 3120.
[80] C. S. Cox and W. Munk, "Statistics of the sea surface derived from sun glitter," *J. Mar. Res.*, vol. 13, no. 2, pp. 198–227, Feb. 1954.
[81] B. A. Hughes and J. L. Grant, "The effect of internal waves on surface wind waves. 1. Experimental measurements," *J. Geophys. Res.*, vol. 83, no. C1, pp. 443–454, Jan. 1978.
[82] B. A. Hughes, "The effect of internal waves on surface wind waves. 2. Theoretical analysis," *J. Geophys. Res.*, vol. 83, no. C1, pp. 455–465, Jan. 1978.
[83] P. A. Hwang and D. W. Wang, "Directional distributions and mean square slopes in the equilibrium and saturation ranges of the wave spectrum," *J. Phys. Oceanogr.*, vol. 31, no. 5, pp. 1346–1360, May 2001.
[84] C. J. Zappa *et al.*, "An overview of sea state conditions and air-sea fluxes during RaDyO," *J. Geophys. Res.*, vol. 117, 2012, Art. no. C00H19.
[85] M. V. Yurovskaya, V. A. Dulov, B. Chapron, and V. Kudryavtsev, "Directional short wind wave spectra derived from the sea surface photography," *J. Geophys. Res.*, vol. 118, pp. 1–15, 2013.
[86] V. Kudryavtsev, M. Yurovskaya, B. Chapron, F. Collard, and C. Donlon, "Sun glitter imagery of ocean surface waves. Part 1: Directional spectrum retrieval and validation," *J. Geophys. Res.*, vol. 122, pp. 1369–1383, 2017.
[87] N. J. M. Laxague, C. J. Zappa, D. A. LeBel, and M. L. Banner, "Spectral characteristics of gravity-capillary waves, with connections to wave growth and microbreaking," *J. Geophys. Res.*, vol. 123, no. 7, pp. 4576–4592, Jul. 2018.

Paul A. Hwang received the B.S. degree in oceanography from the National Taiwan Ocean University, Keelung, Taiwan, in 1973, the M.S. degree in ocean engineering from the University of Rhode Island, South Kingstown, Rhode Island, in 1978, and the Ph.D. degree in civil engineering from the University of Delaware, Newark, DE, USA, in 1982.

After graduate schools, he had postdoctoral training with the Air-Sea Interaction Laboratory, University of Delaware for two and half years. He was a Staff Scientist for four years with Ocean Research and Engineering, Pasadena, CA, USA, one year with Science and Technology, Hampton, VA, USA, and five years with Quest Integrated, Inc., Kent, WA, USA. He joined the Naval Research Laboratory in 1995, first with the Oceanography Division (1995–2006) and currently with the Remote Sensing Division (Since 2006). His research interests include spatial and temporal evolution of ocean surface waves, characteristics of ocean surface roughness, and hydrodynamic aspects of microwave and acoustic remote sensing of the ocean.